Fatigue investigation of a connecting rod in race car engine

K. Bari [a]*, A. Rolfe [a], A. Christofi [a] and C. Mazzuca [a], K.V. Sudhakar [b]

[a] *Department of Mechanical Engineering and the Built Environment, University of Derby, Derby, DE22 3AW, United Kingdom*

[b] *Department of Metallurgical and Materials Engineering, Montana Tech of the University of Montana, Butte, MT 59701, USA*

* Corresponding author at: Room MS 104, Markeaton Street campus, University of Derby, Derby, DE22 3AW, United Kingdom

E-mail address: k.bari@derby.ac.uk

Abstract

In the present work, a failed connecting rod from a motorcycle engine was investigated root cause and also possible mechanisms leading to its premature failure. In addition to finding the root cause, the expectation from this study was to possibly improve the existing designs or practices to avoid similar failures in future. These results were validated using a finite element analysis (FEA) simulation. Scanning electron microscope for investigating the mechanisms of fracture modes, optical microscopy for studying the microstructures and visual inspection were primarily utilised to determine the root cause of the failure. In conclusion, it was determined that the root cause for the premature failure of the connecting rod was the presence of non-metallic inclusions, which led to micro cracking during fatigue loading of the component.

Introduction

A 4-stroke internal combustion engine was used to power a Global GT1 race car. Although commonly used to power Global Class race cars, the engine was not designed for this application. The engine was acquired by the University of Derby after which it was rebuilt. It was then mounted transversely as a stressed member of the GT1 chassis. Throughout its track life, the engine was run at very high speeds, exceeding 11,000 revolutions per minute (RPM). After the engine rebuild, the car had run for around 50 race hours before failing. During a race the engine failed catastrophically with a sudden loss of power. Upon dismantling the engine, a connecting rod was found to have failed along with one of its bolts and its slip bearing. Figure 1a shows a typical connecting rod with key features highlighted and figure 1b shows an intact connecting rod and the failed connecting rod. Connecting rods undergo cyclical tensile and compressive loading during the combustion cycle, suggesting fatigue could be the cause of a failure. At the point of failure, the throttle was being applied, increasing the magnitude of these forces.

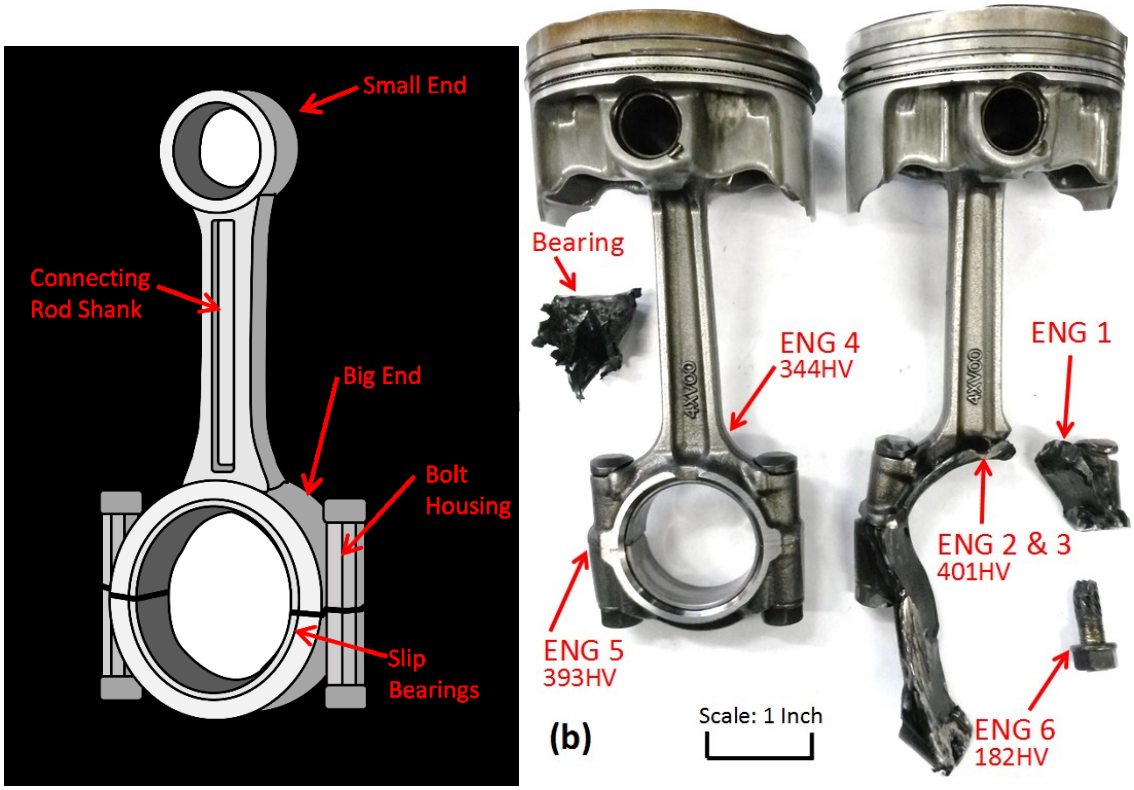


Figure 1:(a) Diagram of an assembled connecting rod, rod cap, bolts and slip bearing with key features and components annotated in red; (b) The intact and failed connecting rod and piston assemblies, left and right consecutively, are shown with the failure.

This study aims to find the mechanism of failure for the failed connecting rod. An investigation was conducted by inspecting the fracture surface, microstructure and hardness of the component and validated using a finite element analysis (FEA) simulation. The failure analysis was conducted in the hope that designs or practices can be improved, and failures such as this avoided in future.

Methodology

A visual inspection was first conducted on the failed components, after they had been removed from the engine, as well as other components such as the oil filter and sump. Statements were also taken from interviews with people involved in refurbishing the car prior to failure. Data from the on-board event data recorder (EDR) was obtained and analysed to accurately assess the condition of the engine during the failure event.

Table 1: Specimen identification system codes and corresponding descriptions for samples analysed.

Specimen Identification	Specimen Description
ENG1	Unmounted failed connecting rod piece consisting of bolt housing and fracture surface.
ENG2	Unmounted section from the top of the failed connecting rod big end with fracture surface.
ENG3	Mounted and polished section from the top of the failed connecting rod big end, corresponding to sample ENG2.
ENG4	Mounted and polished section from the beam of the intact connecting rod.
ENG5	Mounted and polished cross section of a bolt from the intact connecting rod.
ENG6	Mounted and polished cross section of the failed bolt from the failed connecting rod.

Six specimens were collected and tested, ENG1 to 6, some from the failed connecting rod and some from an intact connecting rod from the same failed engine. Each of the rods was sectioned in various places and cross sections of bolts from each connecting rod were also made. One specimen from each of the failed and intact connecting rods as well as the two bolt cross sections were mounted in MetPrep TRI-HARD compound and polished using MetPrep SILICO 0.06 µm colloidal silica paste. The specimen identification system used for all samples is outlined in Table 1 and shown Figure 1.

As part of the fractographic investigation, ENG1 was examined using a limited zoom, full-colour digital microscope; the Nikon ShuttlePix P-400R, to identify areas to be looked at in greater detail using other devices. Polished samples, ENG3 to 6, then went under an Olympus BX51M optical microscope and a digital video recorder was used to capture images of the specimens' microstructures at multiple magnifications.

After identifying key areas to investigate further, most of the fractography was conducted by placing specimens in a scanning electron microscope (SEM); the Zeiss LEO 1550 field emission SEM, to observe surfaces at further magnification. Unmounted samples were cleaned in an ultrasound bath and mounted samples were also etched using 1 M hydrochloric acid, to reveal their microstructures, before entering the SEM. Energy dispersive spectroscopy (EDS) was also conducted on specimens in the SEM to determine chemical composition.

Hardness tests were conducted on mounted samples using an Insize ISH-TDV2000 Vickers hardness tester by applying a 5 kgf force for 5 seconds. An average hardness value was determined by repeating the test 5 times at random locations on each sample surface.

Finally, a finite element analysis (FEA) was conducted to determine the stress distribution in intact connecting rod geometry. The model for these simulations was imported into SolidWorks as a model from a 3D scan taken using a laser camera with some surface modifications. A curvature-based, tetrahedral element mesh was created in SolidWorks from the model. Mesh independent testing was conducted to ensure that results were independent of the mesh density. A uniformly distributed load was applied to 120° of the small end journal, while 180° of the rod cap journal was kept fixed on cylindrical faces, to simulate tension stress in operating conditions.

A reliable mesh was created with about 10^6 parabolic tetrahedral elements, with a uniform global element length of 0.1 mm and a local element length of 0.01 mm at locations with high stress intensity [1]. There were no signs of engine knocking prior to the failure, but during the test sessions the engine reached the highest RPM of 11,000 on at least 5 occasions, and on all laps the engine RPM was frequently close to the RPM limit. The maximum tensile force (14800 N) was calculated from inertia force obtained from the manufacture data listed in the Table 2.

Table 2:Manufacture data of the connecting rod

Crankshaft radius	29 mm
Connecting rod length	141 mm
Piston diameter	70 mm
Mass of the piston assembly	0.234 kg
Mass of the connecting rod	0.239 kg
Stroke length	58 mm
Maximum gas pressure	27.1 bar

Results and Discussion

Visual Analysis

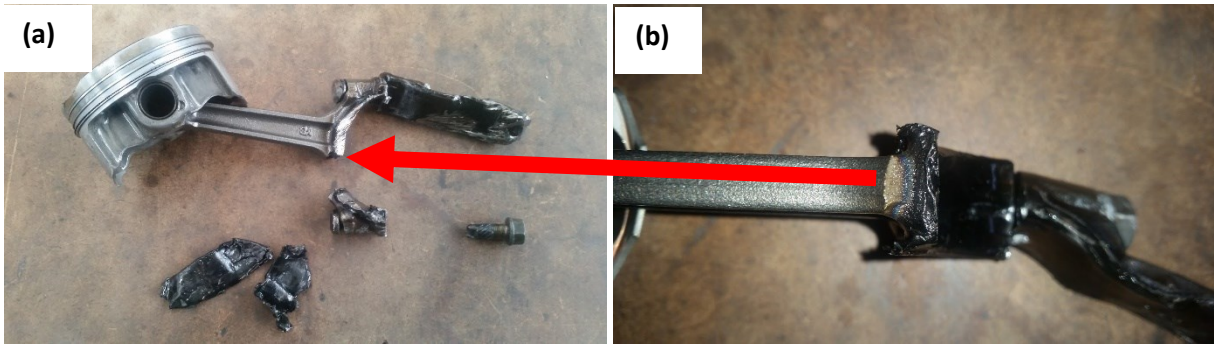


Figure 2:Photographs of the failed connecting rod: (a) Fractured rod shank and big end, fractured rod bolt, deformed rod cap, and melted slip bearing; (b) A closer look of the fracture point highlighted by the red arrow.

Fractography

Figure 2a shows the fracture point at the big end of the connecting rod. The fracture surface (Figure 2b) is normal to the rod big end. Observation of the fracture surface reveals discoloured area due to excessive heat. The rod big end is blackened and it should be noted that the slip bearing is no longer a separate piece; it has melted into the rod big end journal. The rod cap is plastically deformed as shown in Figure 2a. The plastic deformation is due to heat build-up during operation, causing a drop in yield strength leading to the deformation under operational load. Figure 3a shows more close inspection of the blackened rod shank and, presumably by excessive heat. The fracture point of sample ENG-2 shown in Figure 3a reveals deformation via a tensile load, followed by fracture. The fracture point reveal ductile morphology coupled with an angle of shear that is consistent with tensile load fracture. The parabolic dimple effect is also consistent with fracture morphology due to shear loading as shown in Figure 3b. The axial dimple effect in the grain boundaries of the fractured surface is shown in Figure 3c.

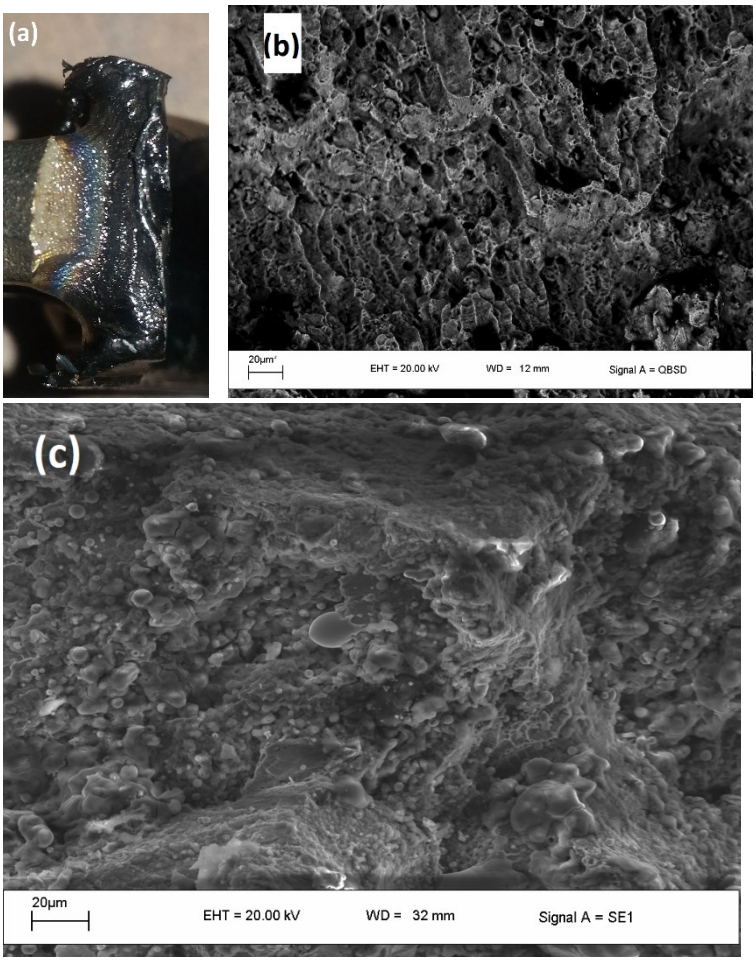


Figure 3: (a) image of failed connection rod; (b) SEM image shows the parabolic fracture point; (C) SEM image shows the axial fracture point.

Evidence of heat tinting was also found, suggesting that thermal hotspots inside the material were a contributing factor to its failure. The blue sections represent a temperature of around 330 °C, the violet represent temperatures of approximately 280 °C, and the yellow areas represent temperatures ranging from 210 °C for the lighter shade to 240 °C for the deeper shade, as seen in Figure 4a [2].

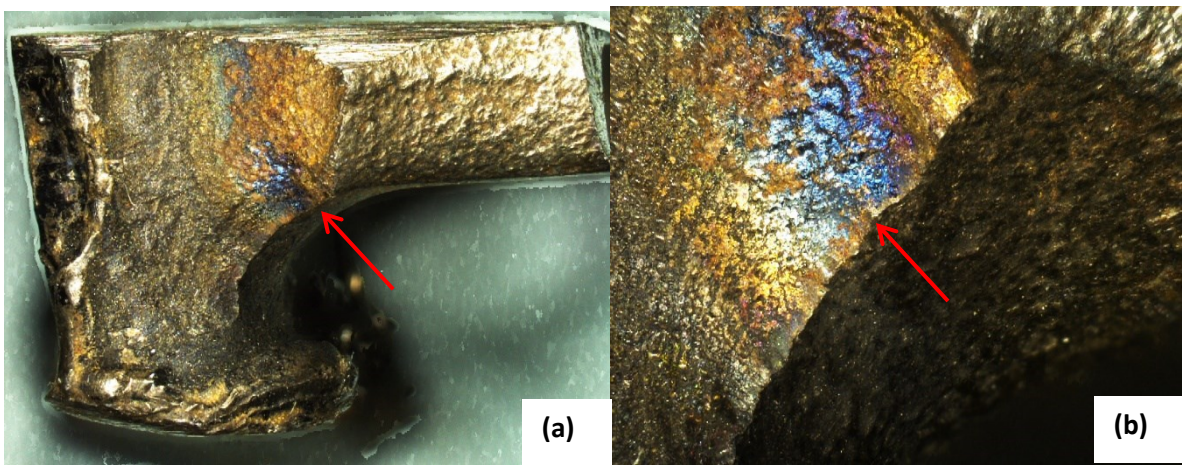


Figure 4: Digital microscope images of ENG1: (a) Digital microscopy reveals heat tinting marks on the fracture surface; (b) Close up showing heat tinting near surface which suggests crack initiation point indicated by the red arrow

Observation of the fracture surface using SEM at the lowest magnification presents key topographies to understanding the cause of fracture including; dimples, chevrons, and a fracture plateau. Beginning with the dimpled region shown in Figure 5, it is shown the geometry of the dimples reveal the direction of the shear, and suggest a micro void coalescence fracture mode. In a micro void coalescence fracture mode, the presence of inclusions or particles create voids. During operation, the voids grow until they reach critical size, at which time they connect and propagate cracking, shearing, or tearing. Using SEM/QBSD imaging of unidentified inclusions can be seen in Figure 7 as bright spots within the black dimpled topography. Void creation takes place at the location of inclusions, therefore suggesting, the dimples on the fracture surface are the site of crack initiation due to the creation of voids from inclusions. The voids lead to a ductile fracture mode shearing towards the fracture plateau. Stemming from the dimpled region multiple chevrons can be seen, highlighted by the yellow arrows in Figure 6. The chevrons emanate from the dimpled region and spread toward the fracture plateau. The direction agrees with the shape and configuration of the dimples confirming the direction of crack propagation from the initiation site of the dimpled region towards the fracture plateau.

The fracture plateau, marked with the red arrow in Figure 5, shows morphology that suggests a brittle fracture mode. The flat, smooth morphology is consistent with brittle fracture morphology seen in many cases including [3]. In a fatigue fracture the final stage is characterized by a rapid fracture, shifting the fracture mode from ductile to brittle. Figure 5 further shows the transition from the dimpled region to the fracture plateau.

Further magnification of SEM imaging of the dimpled region, shown by Figure 8, reveals the mud-type micro cracks that exist on the surface of the connecting rod. These cracks were initiated from sulphur-rich scale layer and harsh environment during race competition [4]. The scale build-up lead to the creation of the voids and allowed for crack propagation. Figure 9 shows a closer investigation of higher magnification of the surface near the fracture point using QBSD mode, which highlight the scale build up in form of iron sulfur-rich scale.

.

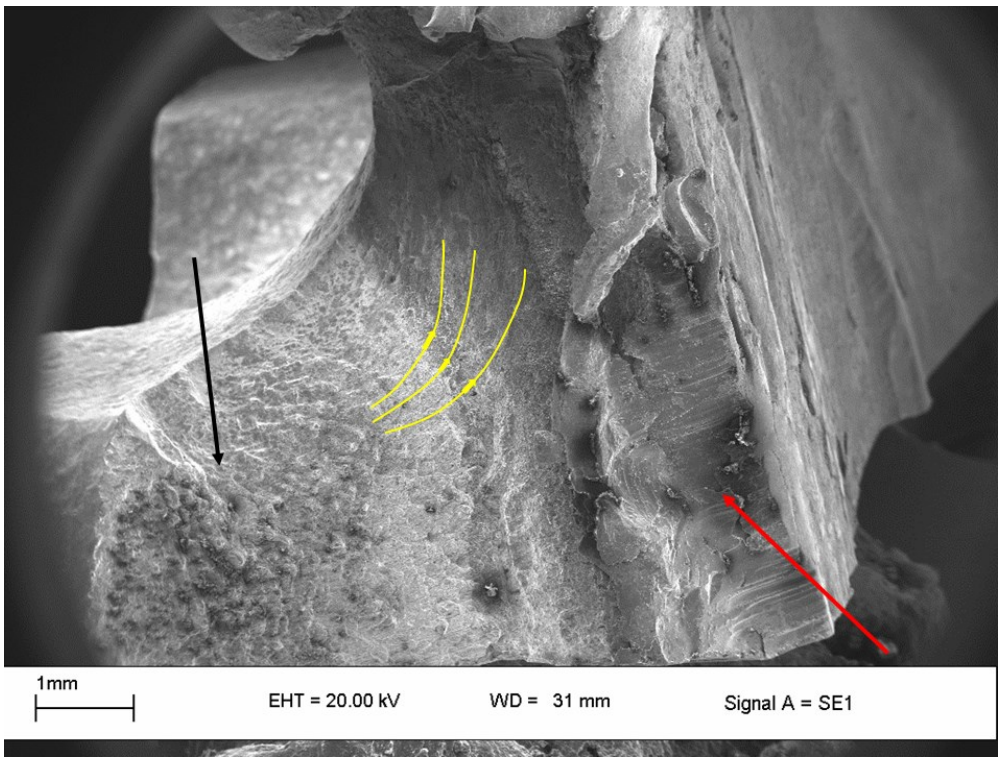


Figure 5:SEM image of the Fracture point in ENG-1

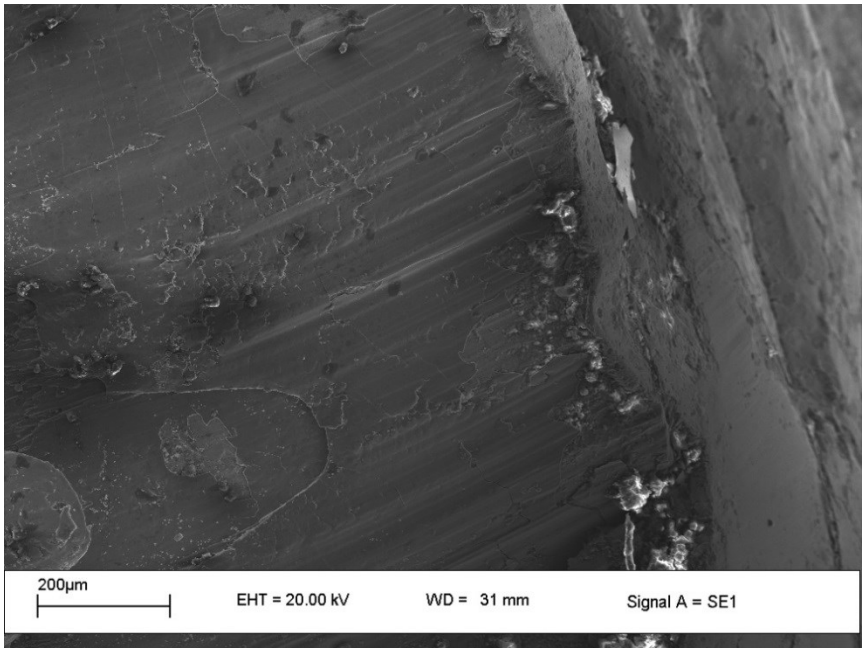


Figure 6:A closer SEM image of fracture surface showing the beach marks

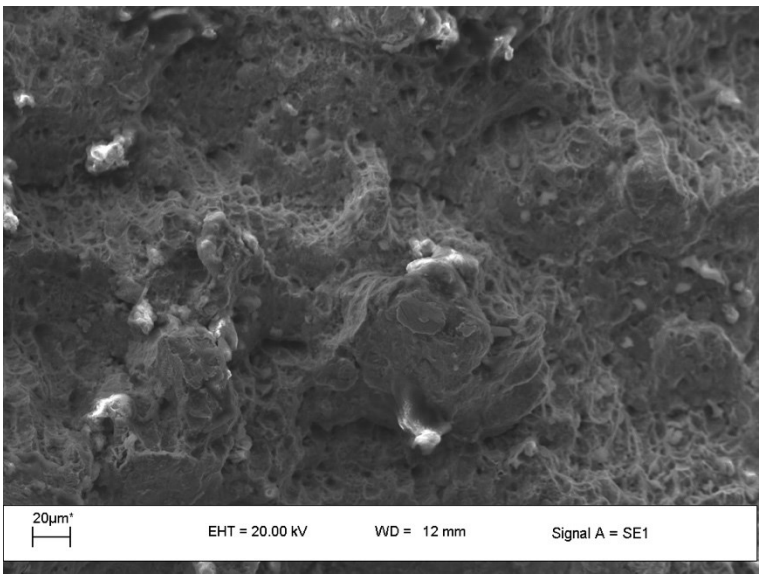


Figure 7:SEM image reveals micro void coalescence fracture mode

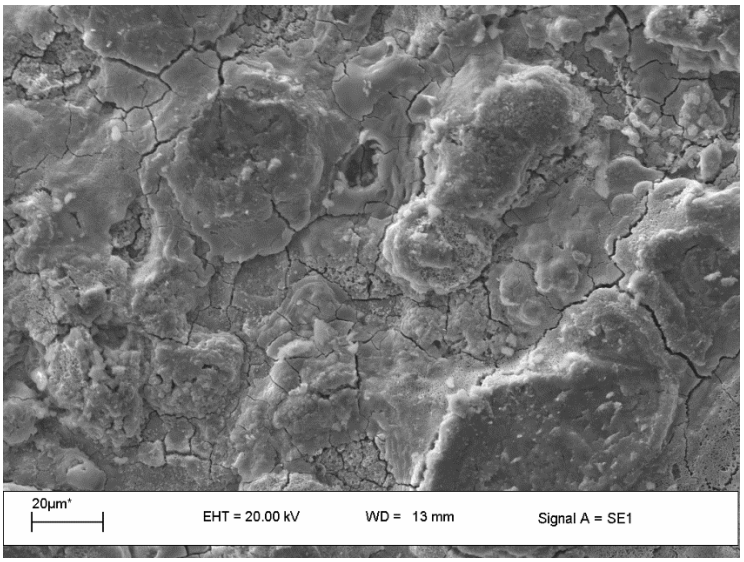


Figure 8: SEM image shows of the micro cracks that appeared near the fracture surface

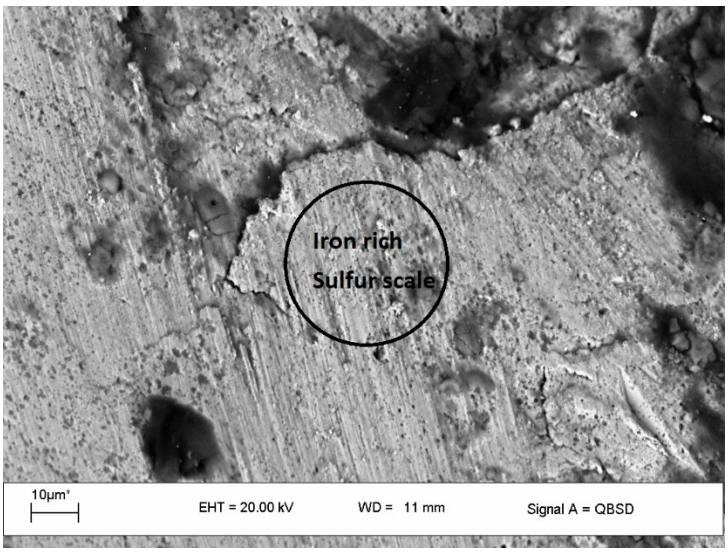


Figure 9: SEM/QBSD image shows the Iron sulfur-rich scale build up on the surface near the fracture point

Hardness Analysis

The hardness test in Table 3 shows that the intact portion of the bolts measured an average of 393 HV, above the maximum hardness for AISI/SAE 4140 medium carbon steel. The fractured bolt measured an average of 182 HV, which indicates that the large reduction in the bolt's hardness shown in Table 3 were due to annealing process caused by overheating the bolt above the it's eutectic temperature. Due to the lower hardness, a spalling effect can be seen inside the bolt hole, making crack initiation much easier.

Table 3:Results of the Vickers hardness tests for the two connecting rod samples measured in Vickers hardness (HV).

Sample	Average Hardness (HV)
Mounted and polished section from the top of the failed connecting rod big end (ENG 3)	401
Mounted and polished section from the beam of the intact connecting rod (ENG 4)	344
Mounted and polished cross section of a bolt from the intact connecting rod (ENG 5)	393
Mounted and polished cross section of the failed bolt from the failed connecting rod (ENG6)	182

Finite Element Analysis

Inertia load is a time-varying quantity and can refer to the inertia load of the connecting rod or of the piston assembly. The maximum tensile load, which is essentially the inertia load of the piston assembly mass, occurs after the firing cycle is completed and a vacuum created in the combustion chamber. It was observed that at high engine speeds, the maximum tension stress in the shank bottom does not occur at the top dead centre (TDC), but at the Bottom dead centre (BDC). It was also observed that the stress ratio varies with location, and at a given location it varies with engine speed. The maximum bending stress over one engine cycle at the shank centre was found to be about 25% of the maximum stress at that location.

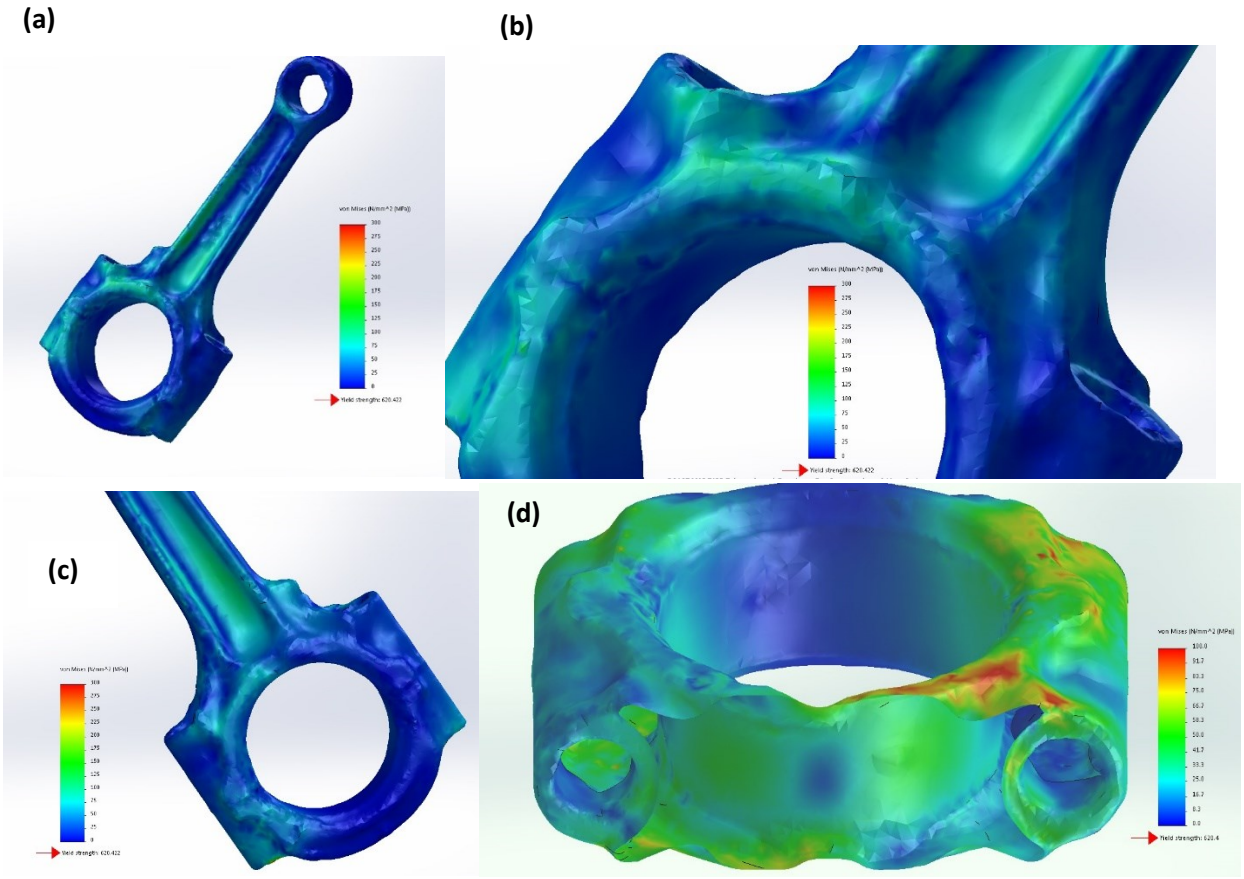


Figure 10: Von-mises stress distribution from FEA simulation: (a) Front view of entire connecting rod; (b) Close-up of big end showing high stress concentration; (c) Rear view of connecting rod big end; (d) Cross sectional view of the connecting rod big end.

After analysing the EDR data, which monitors the engine management system, it was observed that the engine failed suddenly, and lost power during braking and changing down gears into a corner. That means when connecting rod was experiencing the highest tensile stress. The stress analysis in Figure 10a shows that, as expected, the maximum stress region in the model matches the actual fracture and the maximum stress is located between the big end and the shank. Figure 10b and Figure 10c show that average tensile stress at the fracture point was 195 MPa, far below the yield strength of alloy steel, meaning the fracture occurred due to fatigue failure. Figure 10d shows that maximum tensile stresses were located on the surface of the big end, which confirms that surface cracking was the main cause of the failure. Figure 11 shows the statistical fatigue strength of low alloy steel AISI 4140 vs fatigue cycle number obtained from Cambrige Engineering Selector software. The curve in Figure 11 shows the probability of the failure from one million fatigue cycle onward in service at cyclic tension stress of 195 MPa.These fatigue cycle propabilities were based on material imperfection and direction of the acting stress on the crack growth.

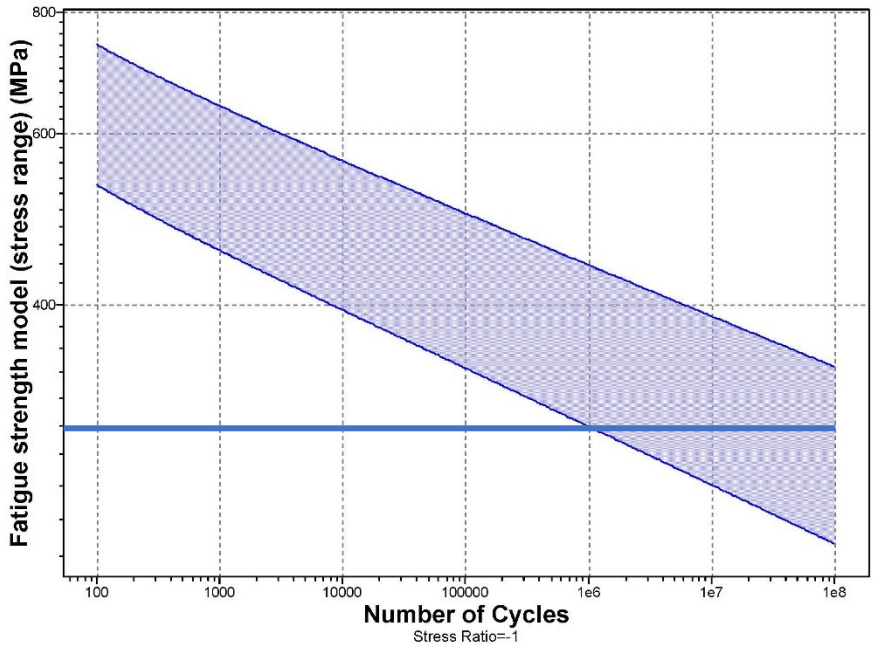


Figure 11:: Graph shows the relationship of probable fatigue strength vs fatigue cycle of Low alloy steel AISI 4140 [5]

Conclusion

The manufacturer's choice of material was made on the design consideration that the engine would be used for street and not race applications, therefore the life expectancy was shortened when the engine was swapped into the Global GT1. Therefore, it had to power a different, heavier chassis. The estimated safe service life of the material at 11,000 RPM is at least 90 minutes according to the one million fatigue cycles obtained in Figure 11. These are sequence of failure modes of the connecting rod:

- The scale-build-up on the steel led to void creation. The voids reached critical size, propagating the crack until the part rapidly fractured. This resulted in a ductile micro void coalescence/ductile fracture mode, and a fatigue failure.
- The heat energy produced by the bearing spinning between the connecting rod's big end and the crankshaft's journal pin caused the connecting rod to overheat, evident from heat tinting marks.
- Observation of the fracture surface reveals fatigue fracture morphology, as similarly observed in failed connecting rods. The fracture reveals ductile and brittle morphologies consistent with fatigue failure.
- It is most likely that the connecting rod failed on the end of exhaust stroke, due to the tensile force being the highest at the end of the exhaust stroke, when the piston reaches TDC. This is due to the inertia of the piston, pin, and upper end of the connection rod moving upwards while there are no compressive forces to take them under consideration.

Acknowledgements

We would like to thank all technicians at the University of Derby and particular Andy Menzies for delivering engine parts and Technical officer for Scanning Electron Microscopy Dr.Graham Souch for his excellent imaging skills.

References

[1] K. Bari, “Characterization of the porosity in TRISO coated fuel particles and its effect on the relative thermal diffusivity,” *Nuclear Engineering and Design,* vol. 265, pp. 668-674, 2013.

[2] Uddeholm, *Temperature guide for tempering steel,* 2015.

[3] S. MacKenzie, “Overview of the Mechanisms of Failure in Heat Treated Steel Components,” *ASM International Failure Analysis of Heat Treated Steel Components,* 2008.

[4] P. Juvonen, “Effects of Non-Metallic Inclusions on Fatigue Properties of Calcium Treated Steels,” 2006.

[5] M. ashby, “www.grantadesign.com,” Cambrige Engineering Selector. [Online]. [Accessed 10 04 2017].

[6] S. Ishida, Y. Hori, T. Kinoshita and T. Iwamoto, “Development of technique to measure stress on connecting rod during firing operation.,” *SAE Technical Paper 951797,* pp. 1851-1856, 1995.

[7] A. Strozzi, A. Baldini, M. Giacopini, E. Bertocchi and S. Mantovani, “A repertoire of failures in connecting rods for internal combustion engines, and indications on traditional and advanced design methods,” *Engineering Failure Analysis,* vol. 60, 2016.

[8] R. Celin, B. Arzensek and D. Kmetic, “A Metallographic Examination of a Fractured Connecting Rod,” *Institute of Metals and Technology,* 2007.